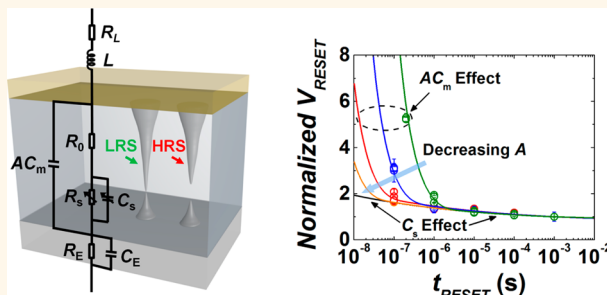# Nanofilament Dynamics in Resistance Memory: Model and Validation

Yang Lu, Jong Ho Lee, and I-Wei Chen*

Department of Materials Science and Engineering, University of Pennsylvania, Philadelphia, Pennsylvania 19104-6272, United States

ABSTRACT Filamentary resistive random-access memory (ReRAM) employs a single nanoscale event to trigger a macroscopic state change. While fundamentally it involves a gradual electrochemical evolution in a nanoscale filament that culminates in an abrupt change in filament's resistance, understanding over many length and time scales from the filament level to the device level is needed to inform the device behavior. Here, we demonstrate the nanoscale elements have corresponding elements in an empirical equivalent circuit. Specifically, the filament contains a variable resistor and capacitor that switch at a critical voltage. This simple model explains several observations widely reported on disparate filamentary ReRAMs. In particular, its collective system dynamics incorporating the power-law time-relaxation of the variable capacitance can accurately account for the responses of variously sized single-filament HfO$_x$ ReRAMs to DC/quasi-static and pulse electrical stimulation, exhibiting Avrami-like switching kinetics and a pulse-rate dependence in on/off voltages.

KEYWORDS: resistance memory · switching dynamics · nanofilaments · Avrami kinetics · relaxation

The demand for high-performance scalable memory devices is stronger today than ever due to the growth of hand-held devices, big-data analysis and cloud storage/computing. Resistive random access memory (ReRAM), which stores "0" and "1" in high resistance state (HRS) and low resistance state (LRS), respectively, is capable of fast switching speed, low operating voltage and high-density 3D integration,[1−3] thus presenting a promising technology. Most ReRAM devices are switched by rupturing and forming conducting nanofilaments in an insulating nanofilm sandwiched between two metal electrodes[4−7] schematically shown in Figure 1a. While many models have been proposed for such devices,[8−12] there is still a need for a generic model that can accurately describe and predict the switching characteristics in all dynamic regimes, from DC/quasi-static testing (*e.g.*, 10^{-3} to 1 s) to fast read/write pulsing (*e.g.*, 10^{-10} to 10^{-7} s). These applications call for a physics-based circuit model with a special focus on nanofilament dynamics. Here we present such a model, depicted in Figure 1a and validated in a prototypical HfO$_x$ bipolar ReRAM over a broad range of sizes, resistance states and excitation/pulse durations.

A useful circuit model ought to have as few variable elements (*i.e.*, voltage/current dependent) as possible. Our model has two, R_s and C_s; together they form the active switching element responsive to excitation. The model is motivated by the following observations. First, previously a simpler version of the model has successfully identified the active element (corresponding to R_s in Figure 1a) inside a bipolar *nonfilamentary* nanometallic ReRAM,[13,14] which switches by a bulk metal−insulator transition.[15−17] It finds switching always occurs at the same critical switching voltage $\pm V^*$ across the active element, even though the apparent switching voltage of the device can vary considerably because additional voltages are borne by inactive elements (the electrode resistor R_E and capacitor C_E, the line resistor R_L and inductor L in Figure 1a.) Therefore, it would be interesting to see if a similar set of critical $\pm V^*$ applies to a filamentary ReRAM, this time across R_s and C_s. Second, regardless of the types of filamentary memory, be it an electrochemical memory (ECM)[18,19] or a valence change memory (VCM),[20,21] its pulse-switching voltage always gradually but persistently rises as the pulse rate increases.[22−30] Several models have been
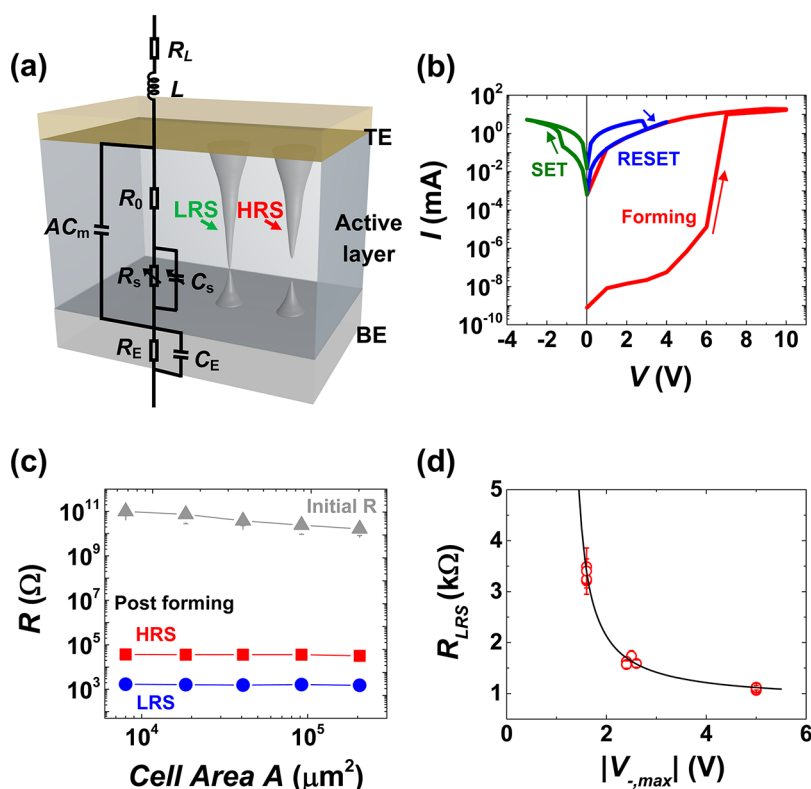
Figure 1. Schematic filamentary ReRAM, its equivalent circuit, and various resistance states. (a) In this metal−insulator−metal structure, a nanofilament opening and closing a variable capacitive gap C_s, in parallel connection with a variable resistance R_s, is responsible for switching between LRS and HRS. The insulator provides a linear capacitor with an area (A) proportional capacitance AC_m. The line resistance R_L, electrode resistance R_E (mostly from the spreading resistance of bottom electrode) and a partial filament resistance R_0 constitute the load. An interfacial capacitance C_E and an inductance L are also included for completeness. (b) After positive-voltage forming (shown in red), $I−V$ curve of bipolar resistive switching follows the arrow direction to SET (shown in green), then RESET (shown in blue). In the forming curve, the postforming hysteresis (red curve at $V > 7$ V) does not overlap, thus allowing different forming voltages to be used to form different HRS. (c) Area dependence of different resistance states under the same forming voltage of 10 V and the same voltage sweeping from −3 to +4 V for switching. Both HRS resistance and LRS resistance are area independent, implying identical-filament switching. (d) Multilevel LRS achieved by different maximum negative voltages in SET ($V_{−,max}$). Each data point is the average of 3 tests (with error bars shown), with 12 data points from 4 size group. Solid curve is model prediction of eq 5 with $V^*_{SET} = -1.2$ V and $R_{load} = 850$ Ω.

proposed to explain this important feature[9−12,24−32] as summarized in Supporting Information, Table S1. However, constrained by their specific mechanisms (*e.g.*, ion migration, atomistic nucleation, and Joule heating), many of these models are limited to a specific memory type (VCM *vs* ECM) or a specific switching direction (on-switching or SET: 0 → 1, *vs* off-switching or RESET: 1 → 0). Therefore, it would be interesting to see whether C_s as an active element can help explain the above ubiquitous feature in disparate devices. Third, the capacitance of a filamentary ReRAM is known to remain constant during switching,[33−37] which has been taken as strong evidence for the filamentary nature. Therefore, we have included a device-area-(A)-proportional capacitor AC_m and attributed it to the inactive dielectric surrounding the nanofilaments. Lastly, the electrode resistor R_E, interfacial capacitor C_E between switching layer and electrodes, line resistor R_L, and line inductor L from the measurement system (*e.g.*, probes and the probe lines) are included in the model for completeness. The values of these circuit elements will be determined by probing a HfO$_x$ ReRAM from

the DC/quasi-DC regime to the fast frequency-time domain.

Before proceeding, it is prudent to question whether this is a realistic model. In principle, during tuning/switching it is possible for a device to gain additional nanofilaments or lose some existing ones. It is also possible that different filaments in the same device or different devices have different characteristics. Obviously, our model requires the ReRAM to maintain an identical set of filaments of identical characteristics at all times. For brevity, we shall refer to this "ideal" case as the single-filament case, though in the context that the "*single-filament*" may mean a "*fixed set of nanofilaments*". A single-filament ReRAM is of practical interest since it has uniform, reliable and predictable switching behavior regardless of size, load, resistance state and form of excitation. Quite possibly, it also presents an attractive nanosystem for other studies and exploration. Below we will report such a ReRAM—with an identical single-filament installed in all the devices of all the sizes and under all the switching conditions. In these devices we shall validate our model.

RESULTS AND DISCUSSION

HfO$_x$ ReRAM with Identical Single-Filament. A HfO$_x$ ReRAM with Ti bottom electrode (BE) and Pt top electrode (TE) was fabricated by HfO$_x$ atomic layer deposition at 250 °C, which left a thin TiO$_x$ layer on Ti with a non-negligible R_E and possibly oxygen deficiencies in HfO$_x$ nanofilm (10 nm thick).[38,39] The virgin HfO$_x$ film is highly resistive as shown in Figure 1b (red), having a device DC resistance of ~10 GΩ. It was "formed' (red curve) by either a positive (Figure 1b, without a current compliance) or negative (Supporting Information, Figure S1, with a compliance) voltage to trigger dielectric breakdown and render nanofilaments in the nanofilm. (In our notation, a positive bias causes a current to flow from TE to BE.) Positive forming left the device in an HRS (Figure 1b), while negative forming left it in an LRS (Supporting Information, Figure S1). Although both are switchable (Figure 1b and Supporting Information, Figure S1), in the following we will focus on positively formed devices which feature highly reproducible, over-lapping switching curves over many cycles (Supporting Information, Figure S2): RESET at approximately +3 V, SET at approximately −1.2 V.

Forming completely changed the scaling behavior of resistance. While before forming the DC resistance decreases linearly with the device size, after forming, the resistance of both HRS and LRS is size-independent if the same forming voltage and test protocol were followed (Figure 1c, where the forming voltage, $V_{f,max}$, was +10 V and the test voltage sweep was from −3 to +4 V.) This is consistent with the single-filament picture: every identically formed device contains a filament of identical characteristic resistance states. By using different forming voltages, different HRS values can be obtained as shown in Supporting Information, Figure S3; nevertheless, the size-independence always holds. Therefore, different forming voltages can be used to tune the characteristics of the single-filament in a series of single-filament devices. This allows us to interrogate (a) the same single-filament in devices of different sizes, and (b) different single-filaments in differently formed devices (having different HRS values). Specifically, we will study 4 different device size groups, each containing devices of 3−5 different size-independent HRS values. (Unless otherwise noted, the HRS and the LRS values refer to their zero-voltage values.)

According to Supporting Information, Figure S3, the size-independent LRS values are relatively insensitive to the forming voltage. However, they do gradually and modestly decrease with $|V_{−,max}|$, the maximum negative voltage used in the sweep. This is illustrated in Figure 1d, where all 12 data points from 4 different size groups fall on the same trend curve. Therefore, devices of 3−4 different LRS values, each covering 4 different size groups, will also be studied.

DC Characterization. In the DC case, the circuit simplifies to Figure 2a having a variable resistance R_s and a constant lumped load $R_{load} = R_0 + R_E + R_L$. Since the apparent switching voltage of the device includes not only $\pm V^*$ but also the voltage on the load, we can use our hypothesis that R_s switches at a critical $V^*_{SET/RESET}$ to solve R_{load} and V^*. (This was previously done for the nanometallic ReRAM.[13,14]) For RESET from the LRS,

$$V^*_{RESET} = \frac{R_s}{R_{LRS}} \times V_{app} = \frac{R_{LRS} - R_{load}}{R_{LRS}} \times V_{app} \quad (1)$$

where V_{app}, the total voltage applied to the circuit at off-switching, and R_{LRS}, the total circuit resistance of the LRS, are experimentally measurable quantities. Comparing

$$\frac{1}{V_{app}} = \frac{1}{V^*_{RESET}} - \frac{R_{load}}{V^*_{RESET}} \times \frac{1}{R_{LRS}} \quad (2)$$

with the experimental data in Figure 2b, we obtain $V^*_{RESET} = 1$ V and $R_{load} = 850$ Ω. Since the plot includes devices from 4 different size groups with 15 data points *in toto*, these best-fit V^*_{RESET} and R_{load} are size-independent and applicable to all LRS values (thus R_s values). In our model, R_L and R_E are constants (R_E being the spreading resistance of a thin conducting film, including both the bottom electrode and the TiO$_x$ film, that are insensitive to electrode size.[40,41]) Therefore, the finding that R_{load} is a constant implies R_0 is too a constant independent of size and resistance state. The above result also makes it clear that the increased V_{app} for off-switching lower-R_{LRS} devices in Figure 2b is due to the load effect and not to any increase in the underlying V^*_{RESET}.

Similarly, for SET from the HRS, the corresponding relation to eq 1 is

$$V_{app} = \frac{R_{HRS}}{R_s} \times V^*_{SET} = \frac{R_{HRS}}{R_{HRS} - R_{load}} \times V^*_{SET} \quad (3)$$

Here, R_{HRS} is the total circuit resistance of the HRS. Expecting $R_{HRS} \gg R_{load} = 850$ Ω, we get $V_{app} \approx V^*_{SET}$. As shown in Figure 2c, which has 4 size groups and 17 data points *in toto*, V_{app} at on-switching is fixed at −1.2 V when R_{HRS} exceeds 10 kΩ. This supports our hypothesis of an invariant V^*_{SET}, of −1.2 V. With the above values for V^*_{SET} and R_{load}, eq 3 is shown as the solid curve in Figure 2c. Thus, V^*_{SET}, R_{load}, and R_0 are all independent of HRS values and device sizes.

Previously, Figure 1d already illustrated how lower LRS values may be obtained, post SET, by ramping the negative sweep to increasingly larger limit, $|V_{−,max}|$. Applying the hypothesis that V^*_{SET} remains at −1.2 V during transitions to these *intermediate* LRS states, we write

$$V^*_{SET} = \frac{R_{LRS} - R_{load}}{R_{LRS}} \times V_{−,max} \quad (4)$$

and

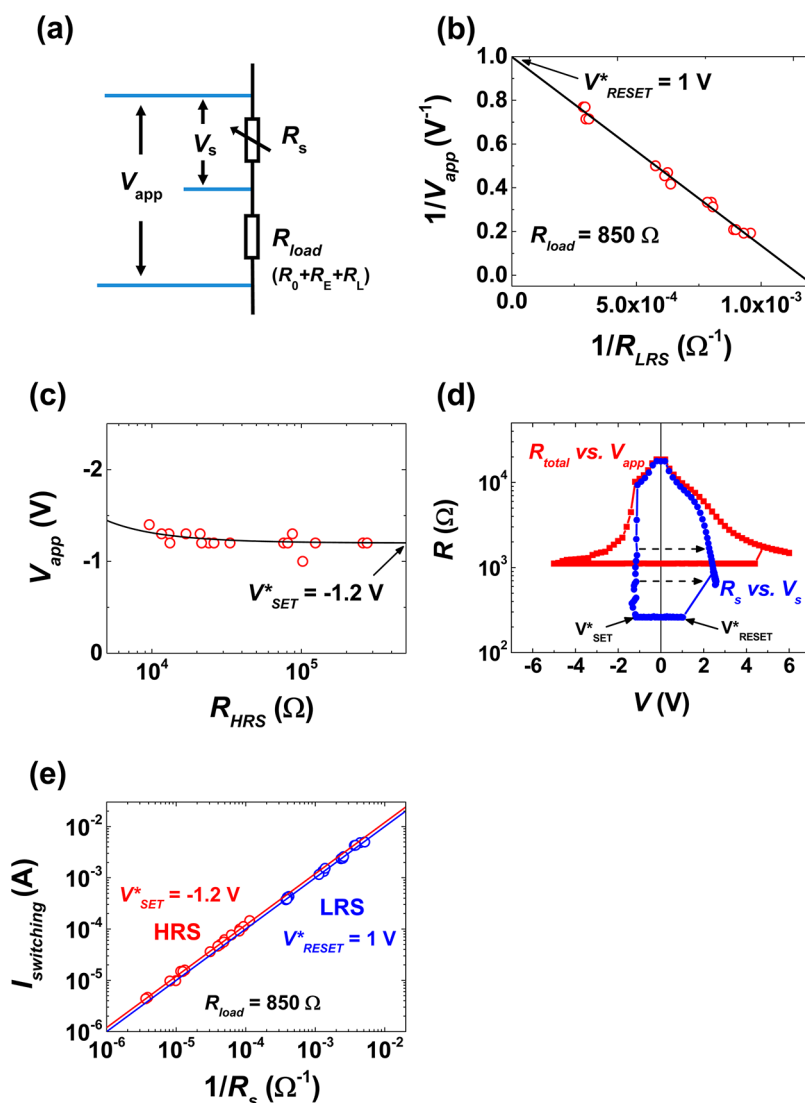$$R_{LRS} = \frac{R_{load}}{1 - \dfrac{V^*_{SET}}{V_{−,max}}} \quad (5)$$

Figure 2. DC switching behavior of single-filament ReRAM. (a) Circuit model in the DC limit: a switching element R_s in the nanofilament in series with load resistance R_{load}, which consists of R_0, R_E, and R_L. (b) Linear fitting using eq 2 to extract model parameters $V^*_{RESET} = 1$ V and $R_{load} = 850$ Ω. Data from 4 size groups, 15 data points in total. (c) V_{app} at on-switching (SET) of different HRS states. Data from 4 size groups, 17 data in total. Solid curve is model prediction of eq 3 with $V^*_{SET} = -1.2$ V and $R_{load} = 850$ Ω. (d) Switching curves represented by R_{total} vs V_{app} from experimentally measurable data, and R_s vs V_s from extracted data. R_s may take any intermediate value between 250 and 8000 Ω. The extreme bipolar switching occurs at $V^*_{RESET} = 1$ V and $V^*_{SET} = -1.2$ V. Data points shown for successive readings of resistance following voltage swept in 0.2 V increment. (e) Switching current of RESET and SET as a function of $1/R_s$. Data from 4 size groups, 30 data in total. Solid lines are model predictions of eq 6 with $V^*_{RESET} = 1$ V, $V^*_{SET} = -1.2$ V, and $R_{load} = 850$ Ω.

With $V^*_{SET} = -1.2$ V and $R_{load} = 850$ Ω, eq 5 gives the smooth curve in Figure 1d in good agreement with the 12 data points. Therefore, the constant-V^* hypothesis is valid for both SET ($V^*_{SET} = -1.2$ V) and RESET ($V^*_{RESET} = 1$ V) for all states and sizes.

According to Figure 2a, R_s differs from the total resistance of the circuit, $R_{LRS/HRS}$, by R_{load}. Given $R_{load} = 850$ Ω, R_s can be directly read from the data of $R_{LRS/HRS}$, at SET/RESET switching voltages and other voltages. Moreover, the voltage on R_s (*i.e.*, V_s) is also known from eqs 1, 3, and 4. Therefore, we can plot in Figure 2d the switching curves of both R_{total} vs V_{app} (both being measurable quantities) and R_s vs V_s (the calculated data, being the voltage on the active element). In the

two extremes, it reveals an Ohmic LRS of 250 Ω, which does not change with voltage, and a HRS of 20 kΩ, which decreases at larger voltages. (At small voltages, HRS is Ohmic; data not shown.) Note that while the LRS abruptly switches—within one voltage increment during the sweep—to HRS at $V^*_{RESET} = 1$ V, the HRS continuously transitions to LRS at a constant V^*_{SET} of -1.2 V. Furthermore, there are intermediate LRS, indicated by the broken arrows, that are also Ohmic and that switch to the same HRS at about $V^*_{RESET} = 1$ V. (Multiple intermediate states are well-known in filamentary ReRAMs; in practice, they are commonly attained by controlling voltage and current, *i.e.*, compliance.[42,43]) With R_s known, a final consistency check is performed on
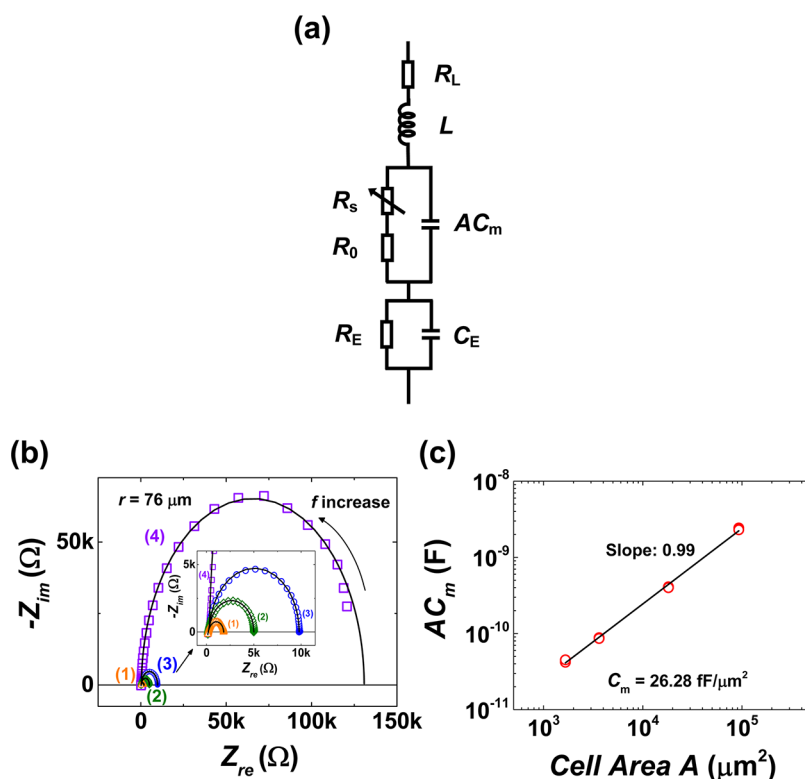
Figure 3. Impedance spectroscopy of filamentary ReRAM. (a) Simplified AC circuit model with one switching element R_s in nanofilament. (b) Impedance spectra of 4 different resistance states of same size (device radius $r = 76\,\mu$m), $R_{LRS/HRS} =$ (1) 2 kΩ, (2) 5 kΩ, (3) 10 kΩ, (4) 130 kΩ, with model fittings (solid curves). Inset: Enlarged view. (c) Extracted film capacitance, AC_m, of 4 size groups each of 4 resistance states (16 data points *in toto*). The slope gives $C_m = 26.28$ fF/μm^2.

RESET/SET current using

$$I_{RESET/SET} = \frac{V_{app}}{R_{LRS/HRS}} = \frac{V^*_{RESET/SET}}{R_s} \qquad (6)$$

Collected from 4 different size groups, the 30 data points in Figure 2e confirm eq 6 and illustrate how the switching current is linearly proportional to $1/R_s$ for both RESET and SET. Here, the SET HRS R_s is taken at the voltage (−1.2 V) just before switching.

Impedance Spectroscopy. The AC response in the frequency domain from 10 Hz to 10 MHz is examined here; the time domain will be studied in the next section. For reasons that will become clear soon, we used a simplified model without C_s, Figure 3a. So the frequency response is directly traced to L, AC_m, and C_E, which are thus determined; we then separate R_E, R_L, and R_0 using $R_0 + R_E + R_L = 850$ Ω. The measured impedance at zero DC bias, including Z_{re} as the real part and Z_{im} as the imaginary part, are represented in the Cole−Cole plot (Figure 3b and Supporting Information, Figure S4), in which the high-frequency limit is the last data point closest to the origin, and the DC resistance is very close to the Z_{re}-axis intercept on the far right. In each plot, such as Figure 3b, spectra of 4 different resistance states from one size are included. Along with the data of 3 other sizes shown in Supporting Information, Figure S4, they are fitted with an identical set of model parameters.

Since the dynamic responses of different lump elements tend to have different RC constants, they tend to segregate into different (frequency) regimes in the Cole−Cole plot. There are two lump elements in Figure 3a, $(R_s + R_0)\|AC_m$ and $R_E\|C_E$. Our fitting reveals that the low frequency spectrum, which is a half-circle arc, is mainly due to $(R_s + R_0)\|AC_m$, while the high frequency spectrum, which is a distorted arc near the origin, is substantially due to $R_E\|C_E$. This also explains, *a posteriori*, why we have ignored C_s: in the above figures, we cannot identify a third regime in which C_s dominates. Later, we will show that because of the C_s dynamics such regime is always so near to the DC limit that it cannot be unambiguously identified. (See Supporting Information, Figure S5 for more information.) At the very high frequency end, we also detected positive Z_{im}, which signifies an inductive contribution. It came from the probes and the probe lines since positive Z_{im} was also seen when the two probe tips were placed in direct contact with each other without touching the device.

From the 16 spectra of 4 different size groups each with 4 DC resistance states, we obtain the best-fit: $L = 3.5\,\mu$H, $R_L = 10$ Ω, $R_E = 340$ Ω and $C_m = 26.28$ fF/μm^2, all being size- and resistance-state-independent; the best-fit C_E, which varies slightly with sizes, is a so-called constant phase element (CPE)[44,45] capacitance with $n \sim 0.5$ and $Q_E \sim 10^{-7}$ Fs^{n-1}. (Setting $n = 0.5$, the

Q_E values for different conditions are given in Supporting Information, Table S2.) In the above fitting of multiple curves, the resistance $R_s + R_0$ is found to vary with the resistance state but not the size. From the values of R_E and R_L, we obtain $R_0 = R_{load} - R_E - R_L = 500\ \Omega$, verifying that R_0 is indeed state and area independent. These values are also tabulated in Supporting Information, Table S2. As shown in Figure 3c, the extracted product AC_m from 16 spectra is proportional to A for the 4 sizes but independent of the DC resistance states, which implies a linear capacitor made of a uniform dielectric with a size- and resistance-state-independent property. Using the above best-fit parameters and the variable R_s from the DC data fitting, we plot the computed spectra as solid black curves in Figure 3a and Supporting Information, Figure S4, all in good accordance with the measured spectra. Lastly, with $C_m = 26.28\ \text{fF}/\mu m^2$ for a layer thickness of 10 nm, the estimated relative dielectric constant ε_r of 29 is reasonable for HfO_x.[46]

Pulse Switching. Pulse excitation is next used to understand the dynamics of nanofilament switching and to provide information on C_s, the only remaining model element not yet determined thus far. Since DC characterization used a time step of 100 ms between successive voltage steps, here we primarily focus on the pulse range from 1 ms to 100 ns, the latter the lower limit to obtain high-fidelity voltage pulses (Figure S6 in Supporting Information) in our measurement system. The results, shown in Figure 4, are summarized below.

First, reminiscent of a trend seen in Figure 2b, Figure 4a shows a larger pulse voltage is required to RESET a less-resistant LRS at a fixed pulse width (t_{RESET}) of 100 ns. (Data of 2 size groups with 3 different t_{RESET} are shown in Supporting Information, Figure S7.) In this experiment, consecutive 100 ns pulses with increasing pulse heights (pulse voltage) were applied to the circuit, and the circuit resistance was read after each pulse at a DC read-voltage of 0.2 V; RESET was declared and V_{RESET} determined when the resistance exceeded 10 kΩ. (More on this choice later.) Second, while the above effect is again seen in Figure 4b comparing different branches of data, the figure shows a time effect on V_{RESET}, which increases with decreasing t_{RESET}. The same trend is seen in other size groups as shown in Figure 4c, in which V_{RESET} is normalized by its 1 ms value to aid comparison. Here, the RESET data are from 4 size groups, each with 2–3 resistance states switched at 5 different t_{RESET} with over 50 data points *in toto*. (Different resistance states in Figure 4c have their normalized V_{RESET} too close to each other to be differentiated.) Third, the time effect is also apparent for SET in Figure 4d. Here, we have determined V_{SET} using a similar protocol for the resistance to fall below 2 kΩ as shown in Supporting Information, Figure S8 for 3 different t_{SET} in 2 size groups, and the normalized data are plotted in Figure 4d, which contains another

50 data points. Meanwhile, the un-normalized pulse-RESET and pulse-SET data are presented in Supporting Information, Figure S9 for various size groups, t_{SET} or t_{RESET} and resistance states. Fourth, switching in a wide $t_{SET/RESET}$ range exhibits the Avrami-like kinetics[47] as shown in Figure 4e,f and Supporting Information, Figure S10: the degree of switching over time follows $1 - \exp(-(t/\tau_0)^p)$ with a strongly voltage (*i.e.*, driving force) dependent relaxation time τ_0, described by a power law $\tau_0 \sim 1/V^q$ or some other voltage function such as $\tau_0 \sim 1/\exp(V^r)$.[48] (Here, p, q and r are positive exponents. More details in caption of Figure 4f and Supporting Information, Figure S11.) Since the switching degree increases with time and voltage, at a fixed voltage the degree increases with $t_{SET/RESET}$ (Figure 4f for RESET, Supporting Information, Figure S10b for SET), and at decreasing $t_{SET/RESET}$, the transition becomes less abrupt and spans over a range of voltage (Figure 4e for RESET, Supporting Information, Figure S10a for SET).

The relaxation time may be used to rationalize three notable features of switching voltage in Figure 4b,c, which are (a) the initial relatively flat V_{RESET} rises suddenly below a threshold t_{RESET}; (b) the threshold t_{RESET} increases with the device size; and (c) before the sudden rise at the threshold, V_{RESET} already gradually rises as the pulse width decreases. These features are also evident in the SET data, Figure 4d. As will be shown below from the relaxation time of the circuit, (a) and (b) are a direct result of AC_m, while (c) may be attributed to C_s that has a time-relaxation dynamics. Consistent with the small voltage increase throughout 1 ms > $t_{SET/RESET}$ > 200 ns in Figure 4c,d, the following analysis will find that the constant V_s hypothesis can be retained and the higher apparent switching voltage attributed to circuit's inability to timely deliver the voltage impulse to R_s and maintaining it. In the analysis, we will ignore C_E and L. (For a CPE element, the equivalent capacitance is roughly estimated as $C_E = (Q_E R_E)^{1/n}/R_E \sim 10^{-11}$ F when combined with a parallel resistor $R_E = 340\ \Omega$, corresponding to a RC time constant in the order of 1 ns, which is outside the range of our study. For $L = 3.5\ \mu H$, its impedance in the time scale of 100 ns switching is less than 10 Ω, which is small enough to be ignored.)

To find the relaxation time of the circuit in Figure 1a, which responds to a heavy sided step-function voltage pulse lasting for $t_s = t_{SET/RESET}$, we conceptually separate the response into two transients: first the pulse charges the capacitor AC_m, next the voltage on the capacitor AC_m charges the capacitor C_s. In each stage, the circuit may be viewed as having a first resistor R_1 connected to a parallel RC unit of a second resistor R_2 and a capacitor C. Solving the standard differential equation that governs the above circuit, we find the product of $R_1 \| R_2$ and C specifies the time required to charge and build up the voltage. This gives two RC time constants as the relaxation times of the
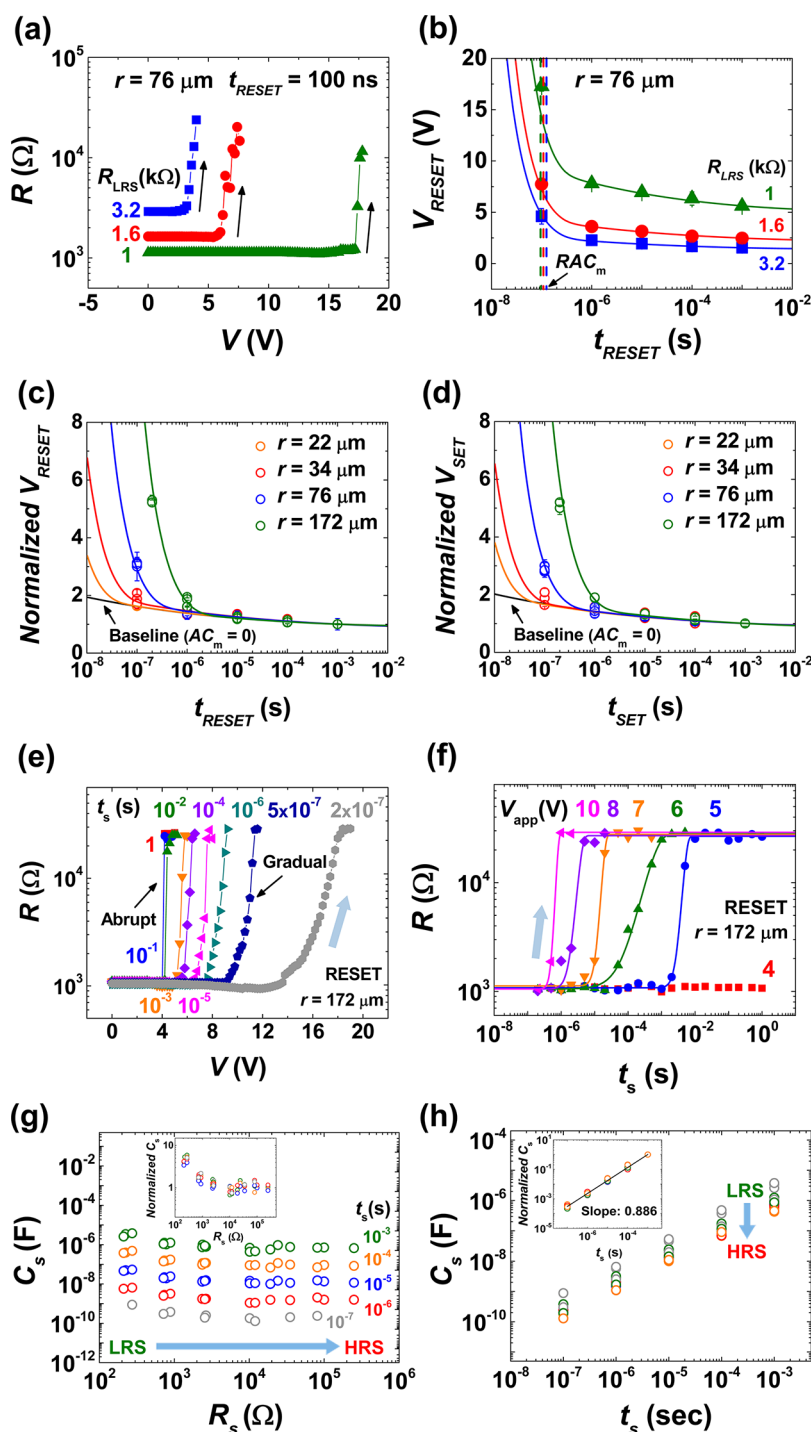
Figure 4. Pulse switching of filamentary ReRAM. (a) DC resistance measured after each 100 ns RESET voltage pulse. Shown for 3 LRS of one size ($r = 76$ μm in device radius). At V_{RESET}, the resistance is switched over 10 kΩ. Arrows indicate the switching direction. (b) V_{RESET} *vs* pulse width (t_{RESET}), for 3 LRS of one size ($r = 76$ μm in device radius). Solid lines are best fit using eq 7 with C_s as the only free variable. Dashed lines: predicted RC time constants. (c) Normalized V_{RESET} (by its value at 1 ms) *vs* t_{RESET}. Data from 4 size groups, each with 2–3 resistance states. Solid curves are best fit using eq 7 with C_s as the only (size-independent) free variable. Black curve labeled "Baseline" assumed vanishing device size to suppress $R - AC_m$ delay. (d) Same as (c) but for V_{SET}, demonstrating the same trend. (e) DC resistance measured after each RESET voltage pulse of various voltages. Shown for t_{RESET} from 200 ns to 1 s, of one size ($r = 172$ μm in device radius). Arrow indicates switching direction. (f) Data of (e) replotted against t_{RESET}, shown for various voltages from 4 to 10 V. Arrow indicates switching direction. Best-fit curves are Arvami kinetics with $p \sim 5$ except $p = 1.46$ for green curve and $r = 0.25$. See text for more detail. (g) Fitted C_s from (c and d) decreases linearly with R_s, then saturates at HRS for various size groups. Nearly overlapping symbols are data from 4 size groups. Inset: normalized C_s (by its value at $R_s \sim 10$ kΩ). RESET/SET voltages analyzed are ones that achieve 10 or 2 kΩ. (h) Same data as in (e). Fitted C_s from (c and d) *vs* pulse width t_s for 6 resistance states each with 4 size groups. (Different sizes not further distinguished because C_s is size-independent.) Inset: normalized C_s (by its value at 1 ms) proportional to $t_s^{0.8858}$. Standard deviation (3 tests) in (c and d) shown as error bar.

circuit: $(R_E + R_L) \| (R_s + R_0) \times AC_m$ in the first stage, and $R_{load} \| R_s \times C_s$ with $R_{load} = R_E + R_L + R_0$ in the second stage. Therefore, we write V_s on R_s and C_s as

$$\frac{V_s}{V_{app}} = \frac{R_s}{R_s + R_{load}} \left[1 - \exp\left(\frac{t_s}{\frac{(R_E + R_L)(R_s + R_0)}{R_L + R_E + R_s + R_0} AC_m} \right) \right]$$
$$\times \left[1 - \exp\left(\frac{t_s}{\frac{R_{load} R_s}{R_{load} + R_s} C_s} \right) \right] \qquad (7)$$

in which the two transient responses are manifest in the two brackets. Riding on the two transients, the voltage on C_s will monotonically increase with time until the applied voltage is removed at time t_s. If by then the voltage V_s on C_s has not reached $V^*_{SET/RESET}$, then there is no switching; if it has already reached $V^*_{SET/RESET}$, then it will have triggered SET/RESET of R_s and C_s at some earlier point and from then on the degree of switching will depend on how much time is left. We thus arrive at the *onset* switching voltage V_{app}: it satisfies $V_s = V^*_{SET/RESET}$ in eq 7 at $t_s = t_{SET/RESET}$. To reach a higher degree of switching, a larger V_{app} is obviously needed.

Utilizing eq 7, we can immediately see that the transient response due to AC_m in the first bracket dictates an A-proportional threshold $t_{SET/RESET}$. The relevant relaxation time is the RC time of the first stage, which has been calculated and marked as dashed lines in Figure 4b. At $t_{SET/RESET}$ shorter than this relaxation time (left of the dashed lines), $V_{SET/RESET}$ rises suddenly, which explains features (a) and (b) above.

Next, we relate feature (c) to the second relaxation time, which is the C_s-related RC time in the second transient. Note that, unlike (a) and (b) which feature a sudden transition across the time scale, feature (c) is rather gradual. This implies the C_s-related RC relaxation time is itself time dependent and roughly commensurate with t_s. Since every quantity in eq 7 except C_s is known from the DC and impedance spectroscopy, we may determine C_s and its time dependence from the V_{app} data for every $t_{RESET/SET}$ and R_s. With one adjustable variable C_s but hundreds of data points over a wide range of size groups, resistance states and pulse widths available, we are able to obtain high-quality fit shown as solid curves in Figure 4b−d and Supporting Information, Figure S9. Here, the fitted V_{app} is higher than the onset V_{app}, because the resistance selected to declare SET/RESET (10 kΩ for RESET and 2 kΩ for SET) well exceeds the onset resistance of switching; a higher degree of switching means "more difficult" switching; thus, it takes a longer relaxation time hence a higher apparent C_s. (See Figure S12 and error analysis in Supporting Information.) However, regardless of the switching degree selected, we find C_s always has the same t_s correlation shown in Figure 4g,h in addition to

a weak R_s correlation shown in the inset of Figure 4g. Fitting normalized C_s (by its values at 1 ms, see inset of Figure 4h) yields the following power-law correlation

$$C_s(R_s, t_s) = C_{s, 1ms}(R_s) \times (t_s/t_0)^{0.8858} \qquad (8)$$

where $t_0 = 1$ ms and $C_{s,1\,ms}$ varies with R_s. Remarkably, although its dynamics, C_s is size-independent: data of 4 different sizes are not distinguishable in these figures.

Before closing this section, we examine two specializations of eq 7. First, when $A \rightarrow 0$, hence $RAC_m \rightarrow 0$, the first bracket becomes 1 and the sudden V_{app} rise due to AC_m is suppressed. In practice, this is realized if $A < 1\ \mu m^2$, then eq 7 predicts a gradual rise of $V_{SET/RESET}$ (black curves in Figure 4c,d labeled as "baseline") encompassing the entire time domain for every size and state in the figures. This baseline gives a complete picture of the feature (c) above, which obviously has nothing to do with the first bracket in eq 7. Second, there is a self-consistency check for eq 7 in the DC $t_s \gg 1$ limit: it reproduces the same relation between V_{app} and V^* as eq 1 in RESET and eq 3 in SET.

DISCUSSION

The above results demonstrate that the present ReRAM regardless of device sizes and states is a single-filament one; and the single-filament has completely identical characteristics except for R_s and C_s, which are individually tunable by forming/testing voltages. As such, the same capacitance (AC_m) is maintained during HRS/LRS conversion, similarly formed and tested devices have the same HRS/LRS values regardless of size, and starting with the same resistance state all the devices switch at the same voltage unless the circuit's R-AC_m response becomes limiting. With only two forming/testing-tunable elements/parameters that are otherwise size-independent, our model can accurately describe the DC, AC and pulse-switching voltage, resistance and capacitance values for numerous devices of various sizes and resistance states. All other circuit elements, R_E, C_E, L, R_0, and C_m, are the same for all devices. In the following, we will discuss the further implications and applications of the nanofilament model in four respects.

(i) Empirical model: Our equivalent circuit is fundamentally an empirical model. As such, it has certain limitations. For example, it cannot distinguish the relative contributions of Pt, Ti and TiO$_x$ to R_E, or whether local Ti oxidation occurs around the nanofilament so that TiO$_x$ resistance enters R_0. Nor can it determine the location of the filament breakage, which may be closer to one electrode or the other, or may even lie inside the transitional conducting layer such as TiO$_x$. While the parameters extracted from the model can serve to constrain the possible mechanisms, some to be examined later in this section, by itself the model cannot determine the mechanism; for example, it does not explain why $|V^*_{SET}|$ is slightly higher than $|V^*_{RESET}|$.

On the other hand, our excellent fit of a large amount of DC and impedance spectroscopy data should lend much confidence to the values of R_E, C_E, L, and C_m, and it is especially remarkable that R_0 and R_s, both belonging to the filament, can be definitely separated. Regarding C_s, while in our model it causes an RC delay that explains the slow but persistent rise in the switching voltage over many orders of pulse time (Figure 4c,d) consistent with the observed switching kinetics (Figure 4e,f), it has such a large magnitude that it probably does not correspond to any physical capacitor in a nanoscale filament, be it a geometric capacitor or an electro-chemical cell, sometimes referred to as a nanobattery or a nanosupercapacitor.[49] Within the empirical model, however, its effect on switching voltage and its dependence on pulse time t_s and R_s can be easily rationalized as follows. First, associating t_s^{-1} with an equivalent switching frequency ω_s, we see the capacitive reactance $|(j\omega_s C_s)^{-1}| \sim \omega_s^{-0.1142}$ gradually falls with ω_s, so the overall impedance and the voltage across $R_s \| C_s$ are reduced, thus necessitating a rise of the V_{app}. Second, as noted before, the equivalent resistance in the RC product in the $t_s \geq 200$ ns domain is $R_1 \| R_2$, with $R_1 = R_{load} = R_0 + R_E + R_L$ and $R_2 = R_s$. Since the normalized $V_{SET/RESET}$ for different resistance states overlap in Figure 4c,d, according to our model these states must have the same RC time. Thus, a smaller R_s in the LRS range requires a larger C_s, a larger R_s in the HRS range requires a smaller and constant C_s. (For HRS, the R_s sensitivity of $R_1 \| R_2$ is very weak because large R_s is shunted by R_1.) Third, with $C_s \sim t_s^\alpha$ where $\alpha = 0.8858$ in our case, it follows that the system (circuit) response demands a gradual rise of switching voltage approximately following $V_{app} \sim t_s^{\alpha-1}$. (This comes from eq 7, $1/V_{app} \sim 1 - \exp(-t_s^{1-\alpha}) \sim t_s^{1-\alpha}$.) Lastly, if we limit the role of C_s entirely to pulse switching, then for self-consistency it should not impact data fitting/analysis of DC and (nonswitching) impedance spectroscopy. This is indeed the model depicted in Figures 2a and 3a, and it is reconfirmed by the calculation in Supporting Information, Figure S5. Therefore, despite its limitations the empirical model is self-consistent in every respect.

(ii) Nonsingle-filament ReRAM: While we used a specific HfO$_x$-based ReRAM to verify our model, the model is not restricted to just such ideal case. Similar model fitting can always be performed on same-size devices that should have the same number of multiple filaments. It is then possible to extract V^*, R_{load}, R_E, R_L, R_0 and R_s, and eq 7 can once again be solved to determine C_s from the pulse-switching data. (Actually, some model parameters such as V^* are easy to obtain even if nanofilaments in a device do change with resistance states in the same cell size. For example, as long as R_{HRS} is much higher than R_{load}, then the SET voltage will not change with the HRS resistance and the extrapolation to obtain V^*_{SET} as in Figure 2c is valid. Next, since $V^*_{RESET} \approx V^*_{SET}$ approximately holds, R_{load} in Figure 2b,c

can be immediately estimated. Using these values together with the results from impedance analysis, C_s in eq 7 is solvable again.) There is another use of our model: because different filaments form parallel elements in the circuit picture, it may be used to analyze parameters of differently sized devices, thus obtaining a definitive measure of their relative filament population. More broadly, while many filamentary ReRAM devices and compositions suffer from highly non-uniform stochastic switching perhaps caused by poor forming practices, our work has amply demonstrated that single-filament devices with little statistical variance are possible. Our forming experience and model analysis further suggest that V^* and R_0 are most likely subject to stochastic variations and have the most impact on V^* and $R_{HRS/LRS}$. Therefore, to incorporate stochastics into modeling, one can first repeat the DC characterization to determine the average V^* and $R_{HRS/LRS}$ along with their statistical variance, then perform the pulse switching analysis after incorporating these statistical features.

(iii) Filamentary vs nanometallic ReRAM: The circuit model and the hypothesis of constant critical switching voltage were previously developed for nanometallic ReRAM, with some similarities and differences as follows. First, highly uniform switching characteristics are most common for nanometallic ReRAM.[16] Therefore, high-quality model fitting similar to the one performed here has been routinely performed for nanometallic ReRAM.[13,14] Second, in nanometallic ReRAM, $R_0 + R_s$ decrease with the device size, while C_m increases with the overall resistance.[17,50] These nonfilamentary features are consistent with a bulk-switching mechanism. Third, nanometallic ReRAM has a rather small or vanishing R_0, allowing its LRS resistance to asymptotically approach R_E when a large $|V_{max}|$ is used. This amplifies the load effect on V_{app} in RESET, allowing $V_{app} \gg V^*_{RESET}$ in some cases.[14] Fourth, the switching voltage of nanometallic ReRAM is completely flat for 20 ns < $t_{SET/RESET}$ < 1 s when the device size is less than 2 μm.[17,50] (The flat switching voltage allows pulse switching to be achieved at 0.1 ps.) Therefore, there is no need to include C_s in a nanometallic ReRAM. (Letting $C_s = 0$ will make the second bracket in eq 7 equal to 1.) Fifth, nanometallic ReRAM does experience a sharp rise of switching voltage at a size-dependent pulse-width, which can be again explained by the RC delay associated with AC_m.[50] Lastly, the constant V^* hypothesis has been fully confirmed for nanometallic ReRAM: V^* is independent of not only the device area but also the device thickness.[17,50] This implies an energy criterion for switching, which is justified because nanometallic ReRAM switching entails charge trapping/detrapping.[17] For filamentary ReRAM, the hypothesis implies switching is dictated by a critical voltage or a critical field, but why such condition holds in an ion-movement-enabled switching device is not

clear. Indeed, the similar V^* condition might suggest some unsuspected underlying commonality between filamentary ReRAM and nanometallic ReRAM.

(iv) Switching models: We close this section by commenting on various switching mechanisms for filamentary ReRAM (see a partial list in Supporting Information, Table S1.) Filamentary switching is generally attributed to ion movement, with possible aids of Joule heating and nonlinear high-field kinetics.[18−21,51] Other considerations such as nucleation and growth of the filamentary/matrix phase have also been invoked.[2,19,29] To assess these mechanisms, one is first reminded of the highly symmetric nature of SET and RESET, e.g., their similar $|V^*|$ values and similarly slow t_s dependence of $V_{SET/RESET}$ for $t_s \geq 100$ ns. Therefore, the controlling mechanism or enabling factor must be a process that can equally effectively proceed in both SET and RESET switching. For example, Joule heating is orders of magnitude more severe during RESET than SET, so on the surface, it cannot be a controlling factor. The asymmetry may be partially ameliorated by recognizing that Joule heating is much more local, thus more effective, in SET where it is generated and dissipated at the ruptured section of the nanofilament as modeled by Ielmini et al. and Bersuker et al.[28,52,53] In this way, some degree of SET/RESET symmetry may be restored but this is by no means generally assured. Second, HRS and LRS are nondegenerate states yet feature highly symmetric two-way transitions. Unlike degenerate-phase transitions for which nucleation-and-growth can explain the symmetric rate-dependence of transition (e.g., the same bipolar coercive field that reversibly moves the interface between oppositely poled ferroelectric domains owes its symmetric rate dependence to thermal nucleation-and-growth of domain-wall steps, kinks and ledges[54]), the interface velocity between nondegenerate phases is generally strongly asymmetric to the driving force (e.g., crystallization requires undercooling but melting does not.[55,56]) Therefore, nucleation-and-growth mechanism is not expected to be equally important for filament connection (SET) and breakage (RESET). Third, any highly nonlinear process that causes the switching rate to be hyper-sensitive to the driving force (aka voltage) may be represented by a switching kinetics that varies as $\exp[(V/V_0)^\nu]$ with $\nu \gg 1$. But if this

is the case, then one should expect $V_{switching}$ to saturate at a certain value after an initial (small) increase with decreasing t_s; a saturation $V_{switching}$ has never been seen in filamentary ReRAM. Lastly, while the critical number of ions deposited/removed required to connect/disconnect a filament can be a symmetric quantity thus making the ion-movement mechanism potentially viable, it is by no means obvious how to achieve this under disparate charge-flow conditions (e.g., the charge passing through the circuit is orders of magnitude larger in RESET than in SET, and orders of magnitude larger when $t_s = 1$ ms than $t_s = 100$ ns). Indeed, defining the efficiency of the ion-movement process as the ratio of ions deposited/removed to the charge passed through, one reaches the seemingly impossible conclusions: (i) the efficiency increases with decreasing t_s, and (ii) the efficiency reaches 100% at a sufficiently short t_s. It is these difficulties of the prevailing mechanisms in the literature that has partially motivated our empirical model; hopefully they will also motivate other future solutions to resolve remaining open questions.

CONCLUSIONS

1. A HfO_x-based single-filament bipolar ReRAM with excellent uniformity and area independence, yet tunable resistance, has been fabricated.

2. The DC switching characteristics and AC impedance spectroscopy of the above devices can be accurately modeled by assigning a device-independent resistance R_0 and a device-dependent tunable resistance R_s—switching at a constant critical voltage V^*—to the filament, in addition to an area dependent capacitance to the surrounding dielectric.

3. In pulse switching, the above device requires a voltage that gradually but persistently increases with decreasing pulse width t_s. This apparently ubiquitous observation for all filamentary ReRAM stems from the Avrami-like kinetics of switching, which can be phenomenologically explained by filament's size-independent RC relaxation time, which increases with time in a sublinear manner.

4. The device dielectric relaxes at an area-proportional RC time, which places an upper limit to the switching speed of all ReRAM.

METHODS

Device Fabrication. ReRAM devices were fabricated on a substrate of thermal-oxide-coated 100 oriented p-type silicon single crystal. A 15 nm Ti bottom electrode was first deposited by e-beam evaporation. Next, a 10 nm HfO_x layer was deposited by ALD at 250 °C using tetrakis(dimethylamido)hafnium (HFDMA) precursor and H_2O. Finally, a 40 nm Pt top electrode was deposited by RF sputtering through a shadow mask, which defined devices from 20 to 200 μm in radius.

Electrical Measurement. Electrical properties were measured using several electrical meters on a Signatone S-1160 probe

station. In a typical test configuration, a bias voltage was applied to the top Pt electrode while the bottom contact was grounded. DC current−voltage (I−V) characteristics were examined using a semiconductor parameter analyzer (SPA, Keithley 237). Impedance measurements were performed using a HP4192A impedance analyzer (10^2 to 10^7 Hz). For pulse RESET/SET switching, an Agilent 81104A pulse generator was used to supply a square-impulse-shaped voltage-pulse train of a constant width but an increasing height (voltage), and a Keithley 237 was used to read the device resistance after each pulse. Switching is considered triggered when the resistance is

switched to a value higher than 10 kΩ (in RESET) or lower than 2 kΩ (in SET).

Supporting Information Available: Additional information on literature and extracted circuit parameters of various sizes and multiple states; positive forming and negative forming; multi-level resistance states; cole—cole plots of various sized devices; impedance spectroscopy fittings with C_s; pulse-switching of various size groups; error analysis. The Supporting Information is available free of charge on the ACS Publications website at DOI: 10.1021/acsnano.5b03032.

REFERENCES AND NOTES

1. Sawa, A. Resistive Switching in Transition Metal Oxides. *Mater. Today* **2008**, *11*, 28–36.
2. Waser, R.; Dittmann, R.; Staikov, G.; Szot, K. Redox-Based Resistive Switching Memories—Nanoionic Mechanisms, Prospects, and Challenges. *Adv. Mater.* **2009**, *21*, 2632–2663.
3. Yang, J. J.; Strukov, D. B.; Stewart, D. R. Memristive Devices for Computing. *Nat. Nanotechnol.* **2013**, *8*, 13–24.
4. Yang, J. J.; Pickett, M. D.; Li, X.; Ohlberg, D. A.; Stewart, D. R.; Williams, R. S. Memristive Switching Mechanism for Metal/Oxide/Metal Nanodevices. *Nat. Nanotechnol.* **2008**, *3*, 429–433.
5. Kwon, D. H.; Kim, K. M.; Jang, J. H.; Jeon, J. M.; Lee, M. H.; Kim, G. H.; Li, X. S.; Park, G. S.; Lee, B.; Han, S.; et al. Atomic Structure of Conducting Nanofilaments in TiO₂ Resistive Switching Memory. *Nat. Nanotechnol.* **2010**, *5*, 148–153.
6. Yang, Y.; Gao, P.; Gaba, S.; Chang, T.; Pan, X.; Lu, W. Observation of Conducting Filament Growth in Nanoscale Resistive Memories. *Nat. Commun.* **2012**, *3*, 732.
7. Chen, J. Y.; Hsin, C. L.; Huang, C. W.; Chiu, C. H.; Huang, Y. T.; Lin, S. J.; Wu, W. W.; Chen, L. J. Dynamic Evolution of Conducting Nanofilament in Resistive Switching Memories. *Nano Lett.* **2013**, *13*, 3671–3677.
8. Ielmini, D.; Nardi, F.; Cagli, C. Universal Reset Characteristics of Unipolar and Bipolar Metal-oxide RRAM. *IEEE Trans. Electron Devices* **2011**, *58*, 3246–3253.
9. Sheridan, P.; Kim, K. H.; Gaba, S.; Chang, T.; Chen, L.; Lu, W. Device and SPICE Modeling of RRAM Devices. *Nanoscale* **2011**, *3*, 3833–3840.
10. Yu, S.; Wong, H. S. Compact Modeling of Conducting-Bridge Random-Access Memory (CBRAM). *IEEE Trans. Electron Devices* **2011**, *58*, 1352–1360.
11. Huang, P.; Liu, X. Y.; Chen, B.; Li, H. T.; Wang, Y. J.; Deng, Y. X.; Wei, K. L.; Zeng, L.; Gao, B.; Du, G.; et al. A Physics-Based Compact Model of Metal-Oxide-Based RRAM DC and AC Operations. *IEEE Trans. Electron Devices* **2013**, *60*, 4090–4097.
12. Linn, E.; Menzel, S.; Ferch, S.; Waser, R. Compact Modeling of CRS Devices Based on ECM Cells for Memory, Logic and Neuromorphic Applications. *Nanotechnology* **2013**, *24*, 384008.
13. Chen, A. B.; Choi, B. J.; Yang, X.; Chen, I. W. A Parallel Circuit Model for Multi-State Resistive-Switching Random Access Memory. *Adv. Funct. Mater.* **2012**, *22*, 546–554.
14. Yang, X.; Chen, I. W. Dynamic-Load-Enabled Ultra-Low Power Multiple-State RRAM Devices. *Sci. Rep* **2012**, *2*, 744.
15. Chen, A. B.; Kim, S. G.; Wang, Y.; Tung, W.-S.; Chen, I. W. A Size-Dependent Nanoscale Metal-Insulator Transition in Random Materials. *Nat. Nanotechnol.* **2011**, *6*, 237–241.
16. Choi, B. J.; Chen, A. B.; Yang, X.; Chen, I. W. Purely Electronic Switching with High Uniformity, Resistance Tunability, and Good Retention in Pt-Dispersed SiO₂ Thin Films for ReRAM. *Adv. Mater.* **2011**, *23*, 3847–3852.
17. Yang, X.; Tudosa, I.; Choi, B. J.; Chen, A. B.; Chen, I. W. Resolving Voltage—Time Dilemma Using an Atomic-Scale Lever of Subpicosecond Electron—Phonon Interaction. *Nano Lett.* **2014**, *14*, 5058–5067.
18. Valov, I.; Waser, R.; Jameson, J. R.; Kozicki, M. N. Electrochemical Metallization Memories—Fundamentals, Applications, Prospects. *Nanotechnology* **2011**, *22*, 254003.
19. Valov, I. Redox Based Resistive Switching Memories (ReRAMs): Electrochemical Systems at the Atomic Scale. *ChemElectroChem* **2014**, *1*, 26–36.
20. Goux, L.; Czarnecki, P.; Chen, Y. Y.; Pantisano, L.; Wang, X.; Degraeve, R.; Govoreanu, B.; Jurczak, M.; Wouters, D. J.; Altimime, L. Evidences of Oxygen-Mediated Resistive-Switching Mechanism in TiN\HfO₂\Pt Cells. *Appl. Phys. Lett.* **2010**, *97*, 243509.
21. Wong, H. S.; Lee, H. Y.; Yu, S.; Chen, Y. S.; Wu, Y.; Chen, P. S.; Lee, B.; Chen, F.; Tsai, M. Metal—Oxide RRAM. *J. Proc. IEEE* **2012**, *100*, 1951–1970.
22. Lee, H. Y.; Chen, P. S.; Wu, T. Y.; Chen, Y. S.; Wang, C. C.; Tzeng, P. J.; Lin, C. H.; Chen, F.; Lien, C. H.; Tsai, M.-J. Low Power and High Speed Bipolar Switching with a Thin Reactive Ti Buffer Layer in Robust HfO₂ Based RRAM. *Int. Electron Devices Meet.* **2008**, 1–4.
23. Govoreanu, B.; Govoreanu, B.; Kar, G. S.; Chen, Y.; Paraschiv, V.; Kubicek, S.; Fantini, A.; Radu, I. P.; Goux, L.; Clima, S.; et al. 10 × 10nm² Hf/HfOₓ Crossbar Resistive RAM with Excellent Performance, Reliability and Low-Energy Operation. *IEEE Int. Electron Devices Meet.* **2011**, 31–6.
24. Menzel, S.; Waters, M.; Marchewka, A.; Böttger, U.; Dittmann, R.; Waser, R. Origin of the Ultra-Nonlinear Switching Kinetics in Oxide-Based Resistive Switches. *Adv. Funct. Mater.* **2011**, *21*, 4487–4492.
25. Yu, S.; Wu, Y.; Wong, H. S. P. Investigating the Switching Dynamics and Multilevel Capability of Bipolar Metal Oxide Resistive Switching Memory. *Appl. Phys. Lett.* **2011**, *98*, 103514.
26. Kim, K. M.; Jeong, D. S.; Hwang, C. S. Nanofilamentary Resistive Switching in Binary Oxide System; a Review on the Present Status and Outlook. *Nanotechnology* **2011**, *22*, 254002.
27. Medeiros-Ribeiro, G.; Perner, F.; Carter, R.; Abdalla, H.; Pickett, M. D.; Williams, R. S. Lognormal Switching Times for Titanium Dioxide Bipolar Memristors: Origin and Resolution. *Nanotechnology* **2011**, *22*, 095702.
28. Ielmini, D.; Nardi, F.; Balatti, S. Evidence for Voltage-Driven Set/Reset Processes in Bipolar Switching RRAM. *IEEE Trans. Electron Devices* **2012**, *59*, 2049–2056.
29. Tsuruoka, T.; Hasegawa, T.; Valov, I.; Waser, R.; Aono, M. Rate-Limiting Processes in the Fast SET Operation of a Gapless-Type Cu-Ta₂O₅ Atomic Switch. *AIP Adv.* **2013**, *3*, 032114.
30. Strachan, J. P.; Torrezan, A. C.; Miao, F.; Pickett, M. D.; Yang, J. J.; Yi, W.; Gilberto, M. R.; Williams, R. S. State Dynamics and Modeling of Tantalum Oxide Memristors. *IEEE Trans. Electron Devices* **2013**, *60*, 2194–2202.
31. Yu, S.; Wong, H. S. P. A Phenomenological Model for the Reset Mechanism of Metal Oxide RRAM. *IEEE Electron Device Lett.* **2010**, *31*, 1455–1457.
32. Larentis, S.; Nardi, F.; Balatti, S.; Gilmer, D. C.; Ielmini, D. Resistive Switching by Voltage-Driven Ion Migration in Bipolar RRAM—Part II: Modeling. *IEEE Trans. Electron Devices* **2012**, *59*, 2468–2475.
33. You, Y. H.; So, B. S.; Hwang, J. H.; Cho, W.; Lee, S. S.; Chung, T. M.; Kim, C. G.; An, K. S. Impedance Spectroscopy Characterization of Resistance Switching NiO Thin Films Prepared through Atomic Layer Deposition. *Appl. Phys. Lett.* **2006**, *89*, 222105.
34. Jeong, D. S.; Schroeder, H.; Waser, R. Impedance Spectroscopy of TiO₂ Thin Films Showing Resistive Switching. *Appl. Phys. Lett.* **2006**, *89*, 082909–082909.
35. Yu, S.; Jeyasingh, R.; Wu, Y.; Wong, H. S. P. AC Conductance Measurement and Analysis of the Conduction Processes in HfOₓ Based Resistive Switching Memory. *Appl. Phys. Lett.* **2011**, *99*, 232105.

36. Jiang, X. L.; Zhao, Y. G.; Chen, Y. S.; Li, D.; Luo, Y. X.; Zhao, D. Y.; Sun, Z.; Sun, J. R.; Zhao, H. W. Characteristics of Different Types of Filaments in Resistive Switching Memories Investigated by Complex Impedance Spectroscopy. *Appl. Phys. Lett.* **2013**, *102*, 253507.

37. Yoon, J. W.; Yoon, J. H.; Lee, J. H.; Hwang, C. S. Impedance Spectroscopic Analysis on Effects of Partial Oxidation of TiN Bottom Electrode and Microstructure of Amorphous and Crystalline HfO$_2$ Thin Films on Their Bipolar Resistive Switching. *Nanoscale* **2014**, *6*, 6668–6678.

38. Lee, H. Y.; Chen, Y. S.; Chen, P. S.; Wu, T. Y.; Chen, F.; Wang, C. C.; Tzeng, P. J.; Tsai, M. J.; Lien, C. Low-Power and Nanosecond Switching in Robust Hafnium Oxide Resistive Memory with a Thin Ti Cap. *IEEE Electron Device Lett.* **2010**, *31*, 44–46.

39. Lin, Y. S.; Zeng, F.; Tang, S. G.; Liu, H. Y.; Chen, C.; Gao, S.; Wang, Y. G.; Pan, F. Resistive Switching Mechanisms Relating to Oxygen Vacancies Migration in Both Interfaces in Ti/HfO$_x$/Pt Memory Devices. *J. Appl. Phys.* **2013**, *113*, 064510.

40. Dickens, L. E. Spreading Resistance as a Function of Frequency. *IEEE Trans. Microwave Theory Tech.* **1967**, *15*, 101–109.

41. Timsit, R. S. Constriction Resistance of Thin Film Contacts. *IEEE Trans. Compon. Packag. Technol.* **2010**, *33*, 636–642.

42. Liaw, C.; Kund, M.; Schmitt-Landsiedel, D.; Ruge, I. The Conductive Bridging Random Access Memory (CBRAM): A Non-Volatile Multi-Level Memory Technology. *ESSDERC 2006, Proc. Eur. Solid-State Device Res. Conf., 37th* **2007**, 226−229.

43. Prakash, A.; Park, J.; Song, J.; Woo, J.; Cha, E. J.; Hwang, H. Demonstration of Low Power 3-bit Multilevel Cell Characteristics in a TaOx-Based RRAM by Stack Engineering. *IEEE Electron Device Lett.* **2015**, *36*.

44. Raistrick, I. D.; Franceschetti, D. R.; Macdonald, J. R. *Impedance Spectroscopy: Theory, Experiment, and Applications, Second Edition*; Wiley-Interscience: Hoboken, NJ, 2005; pp 27−128.

45. Hirschorn, B.; Orazem, M. E.; Tribollet, B.; Vivier, V.; Frateur, I.; Musiani, M. Constant-Phase-Element Behavior Caused by Resistivity Distributions in Films I. Theory. *J. Electrochem. Soc.* **2010**, *157*, C452–C457.

46. Wilk, G. D.; Wallace, R. M.; Anthony, J. M. High-κ Gate Dielectrics: Current Status and Materials Properties Considerations. *J. Appl. Phys.* **2001**, *89*, 5243–5275.

47. Avrami, M. Kinetics of Phase Change. I General Theory. *J. Chem. Phys.* **1939**, *7*, 1103–1112.

48. Avrami, M. Kinetics of Phase Change. II Transformation-Time Relations for Random Distribution of Nuclei. *J. Chem. Phys.* **1940**, *8*, 212–224.

49. Valov, I.; Linn, E.; Tappertzhofen, S.; Schmelzer, S.; Van den Hurk, J.; Lentz, F.; Waser, R. Nanobatteries in Redox-Based Resistive Switches Require Extension of Memristor Theory. *Nat. Commun.* **2013**, *4*, 1771.

50. Yang, X. *Resistance Switching Devices Based on Amorphous Insulator-Metal Thin Films*. Ph.D. Dissertation, University of Pennsylvania, 2014. arXiv:1412.2083.

51. Song, S. J.; Seok, J. Y.; Yoon, J. H.; Kim, K. M.; Kim, G. H.; Lee, M. H.; Hwang, C. S. Real-time Identification of the Evolution of Conducting Nano-filaments in TiO$_2$ Thin Film ReRAM. *Sci. Rep.* **2013**, *3*, 3443.

52. Ielmini, D. Modeling the Universal Set/Reset Characteristics of Bipolar RRAM by Field-and Temperature-Driven Filament Growth. **2011**, *58*, 4309−4317.

53. Bersuker, G.; Gilmer, D. C.; Veksler, D.; Kirsch, P.; Vandelli, L.; Padovani, A.; Larcher, L.; McKenna, L.; Shluger, A.; Iglesias, A.; et al. Metal Oxide Resistive Memory Switching Mechanism Based on Conductive Filament Properties. *J. Appl. Phys.* **2011**, *110*, 124518.

54. Shin, Y. H.; Grinberg, I.; Chen, I. W.; Rappe, A. M. Nucleation and Growth Mechanism of Ferroelectric Domain-Wall Motion. *Nature* **2007**, *449*, 881–884.

55. Uhlmann, D. R.; Bowen, H. K.; Kingery, W. D. *Introduction to Ceramics*, 2nd ed; Wiley: New York, 1976; p 346.

56. Meiling, G. S.; Uhlmann, D. R. Crystallization and Melting Kinetics of Sodium Disilicate. *Phys. Chem. Glasses* **1967**, *8*, 62.